Modeling of Near-Well Matrix Acidization

A. R. Shaik[1], P. Y. Tomin[2], and D. V. Voskov[1,2]

[1]Department of Geoscience & Engineering, TU Delft, Stevinweg 1, 2628 CN Delft, Netherlands
[2]Department of Energy Resources Engineering, Stanford University, Stanford, CA 94305, USA
D.V.Voskov@tudelft.nl

Keywords: LEGERs, matrix acidization, Darcy-Brinkman-Stokes, wormholes, AD-GPRS

ABSTRACT

The growing global energy consumption and drive for cleaner energy have generated an immense interest in low enthalpy geothermal energy resources (LEGERs) as an alternative and readily available resource. The LEGERS, albeit under 100 °C, can be harvested to provide heating and power generation from household to industrial scale. One of the challenges encountered during the exploration of such geothermal reservoirs is a poor hydraulic connectivity between the wells. Another challenge is the natural precipitation of solids which leads to an additional permeability reduction, i.e. formation damage. While these problems can be solved by a hydraulic stimulation, the application of chemical stimulation is another clear alternative. In our study, we model an acid stimulation in the near-well region at a high resolution and directly resolve the shape of wormholes associated with matrix dissolution. Since this region has a significant impact on the efficiency of the entire stimulation job, it is of great importance to capture this phenomenon accurately. In the high-resolution simulation study, the solid matrix in some control volumes can be fully dissolved by acid. Since the canonical Darcy's law cannot be applied when the porosity is near unity, a single, unified continuum approach namely the Darcy-Brinkman-Stokes (DBS) equation is employed and compared with Darcy model. The simulations are done using the Automatic Differentiation General Purpose Research Simulator (AD-GPRS). A convergence analysis and sensitivity studies are performed for key parameters to fully describe and understand the behavior. The shape of wormholes is studied for different flow rates and is validated against a published work for both Darcy and DBS models. The wormholes characteristics, obtained in these two models, are defined by breakthrough parameters and dimensionless variables. Convergence analysis and sensitivity studies were performed for several parameters to fully describe and understand the differences in 2D systems.

1. INTRODUCTION

The near-well area is the most accurately characterized region of the subsurface porous media. Most logging tools capture the data such as porosity, resistivity, density, and sonic time up to a high degree of accuracy, hence making the near borehole area well distinguished. This detailed description can be used for an accurate study of different processes related to well productivity. Based on these studies, we can predict and further optimize the performance of the well and in addition propose more accurate models for the large-scale representation of well.

Another reason why the study of the near-well area is of considerable importance is its impact on the overall pressure profile during extraction. In a radial flow well, the first 20 ft accounts for 50% flowing pressure gradient drop and just the first 3 ft account for 25% of it. If these near well areas are affected by formation damage, it could have a pronounced effect on well performance (Kalfayan, 2008). To remove formation damage due to clogging of the pores and to restore and improve permeability, acid stimulation is employed. If the acid is injected at a pressure above the fracture gradient, it is called fracture acidizing. The acid propagates across the face of the fracture and penetrates deep into the reservoir. Another strategy is to pump the acid into the reservoir below the formation pressure so that the acid flows, dissolving the damage through the reservoir via the existing pores and the natural fractures. This strategy is known as matrix acidizing and it is studied in this work.

Acid stimulation is one of the most employed techniques used in subsurface engineering. The first patent for an acid job dates back to 1896 (Crowe and Thomas, 1992), and it is still a widely used industry practice with a century after it was conceived. In 1994, 79% of the stimulation jobs in the petroleum industry were comprised only of acid stimulation (Earlougher Jr, 1977). Today, this technology is widely employed in multiple industrial activities including some geothermal projects (Barrios et al., 2002; Jaimes-Maldonado and Sanchez-Velasco, 2003).

The growing global energy consumption and drive for cleaner energy has generated an immense interest in low enthalpy geothermal energy resources (LEGERS) as an alternative and readily available resource. These resources, albeit under 100 ℃, can be harvested to provide heating and power generation from household to industrial scale. One of the challenges encountered during the exploration of such geothermal reservoirs is the poor hydraulic connectivity of wells caused by drilling mud. A related and critical challenge is the natural precipitation of rock which leads to a permeability reduction i.e. formation damage in the near-well area. Although hydraulic stimulation along the entire reservoir can be applied to improve the efficiency of such wells, the application of

chemical stimulation to the near-well region can also be effective without risks posed by fracking. There are strong similarities between hydrocarbon and low enthalpy geothermal reservoirs in terms of extraction, injection and well optimization methods including matrix acidizing (Xydis et al., 2013; Portier et al., 2009).

Accurate modeling can help in a better identification of risks and suggests optimal operational regimes. However, having the most accurate characterization of a near wellbore area will not automatically guarantee that the subsurface simulation will be predictive. The results of modeling are usually very sensitive to the accuracy of representation of physical phenomena associated with the processes of practical interest. For the chemical processes which include a dissolution of rock material, the problem arises with the predictive representation of flow.

Taking into account the spatial scale of discretization, some of simulation control volumes can have values of porosity close to 1, which makes the usual usage of Darcy's law wrong and requires employing Stokes equation for description of flow in such grid blocks. The unified Darcy-Brinkman-Stokes (DBS) equation provides an opportunity to describe such phenomena by automatically switching the description between Darcy velocities in control volumes with low porosity and velocities controlled by Stokes equation in high porosity grid blocks. The adjustment of porosity due to a chemically driven dissolution is directly accounted in the framework. In this work, we performed a detailed study and comparison between Darcy and DBS models based on numerical implementation in Automatic Differentiation General Purpose Research Simulator (AD-GPRS) (AD-GPRS, 2017; Rin et al., 2017; Rin, 2017).

2. MATHEMATICAL DESCRIPTION

The governing equations for reactive transport involve a combination of mass conservation, momentum conservation, and kinetic reaction model for chemical species. A two-phase model of solid (s) and fluid phase (f) is considered with water, acid, reaction product, and solid components. In this study, we assume an incompressible flow in the absence of capillary or gravity effects.

Molar variable formulation is used to solve the governing equations, as described in Voskov and Tchelepi (2012), Farshidi, (2016). The coupled system of equations is spatially discretized employing a finite-volume scheme with a two-point flux approximation. The non-linearities are handled using Newton's method and the resulting linear matrix system is solved using the Parallel Sparse Direct Solver (PARDISO) (Schenk and Gärtner, 2004).

2.1. Conservation of Species

Mass conservation equation for i^{th} component in fluid phase is given by

$$\frac{\partial}{\partial t}(\phi \rho_f z_i) + \nabla \cdot (\rho_f z_i \mathbf{V} - \phi \rho_f D_i \nabla z_i) = v_i r \tag{1}$$

where:

- z_i – mole fraction of ith component,
- ρ_f – molar density of fluid phase,
- D_i – diffusion coefficient,
- $\mathbf{V}$ – velocity of fluid phase,
- v_i – stoichiometric coefficient for i^{th} component,
- r – reaction rate.

The solid species are dissolved into the fluid phase and the solid concentration decay can be accounted as

$$\frac{\partial C_s}{\partial t} = v_s r \tag{2}$$

where C_s is the solid concentration over the control volume (Fan et al., 2010, 2012; Farshidi et al., 2013). Note that the fluid component concentrations are defined over the net fluid (= pore) volume and the solid concentration is defined over the entire control volume which includes fluids and solids.

2.2. Momentum Conservation

Usually the relationship between pressure and velocity is given by the canonical Darcy's law (Darcy, 1856). The velocity of the fluid phase is given by

$$\mathbf{V} = -\frac{K}{\mu}\nabla P \tag{3}$$

Strictly speaking, it is incorrect to apply Darcy's Law in regions with near 100% porosity, the simulation model obtained with Darcy's is not accurate as the Stokes' model should be used for an open channel flow. One way to avoid this shortcoming is to allocate regions with high porosity and apply Stokes' equations there when Darcy's law can be applied elsewhere. However, this approach requires a complicated tracking of the boundaries of these regions to preserve continuity.

Instead, one can employ the Darcy-Brinkman-Stokes' (DBS) equation (Brinkman, 1949; Soulaine and Tchelepi, 2016). The key difference between the Darcy model and the Darcy-Brinkman-Stokes (DBS) model is the handling of control volumes with high porosity. DBS is a unified, single domain approach that inherently takes into account the amount of solid phase in the control volume. The DBS equation is given by

$$\nabla P + \frac{\mu}{K}\mathbf{V} - \frac{\mu}{\phi}\mathbf{V} = 0 \tag{4}$$

The third term in the equation describes fluid-fluid viscous forces. In contrast to the Stokes' equation, the viscosity is no longer μ but an effective viscosity given by μ/ϕ. The fluid does not have its original viscosity on account of momentum dispersion as reported by Vafai (2015) (Chapter 3, P. 100). Although there is no clear consensus on the application of effective viscosity (Nield and Bejan, 2006), numerical simulations done by Ochoa-Tapia and Whitaker (1998) confirm that the effective viscosity is indeed increased by a multiplier of $1/\phi$. Hence, this modification was done to the Brinkman equation consistent with other experimental and simulation works (Goyeau et al., 2003; Bousquet-Melou et al., 2002; Hsu and Cheng, 1990; Vafai and Tien, 1981; Soulaine and Tchelepi, 2016; Soulaine et al., 2016, 2017).

2.3. Chemical Reactions

For simplicity, we limit consideration to a single chemical reaction, which is assumed to be a simple first order kinetic reaction consistent with dissolution of rock with acid

$$\text{Acid} + \text{Solid} \rightarrow \text{Product},$$
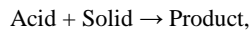
where the reaction rate is given by

$$r = \alpha C_s z_{acid} \tag{5}$$

Here α is the reaction rate constant and z_{acid} is the acid concentration.

2.4. Constitutive Relations for Porosity and Permeability

The distinctive feature of reactive transport in comparison with normal single phase flow is that the porosity and permeability fields are no longer constant and must be updated as the acid dissolves the carbonate matrix. This porosity increase has a direct relationship with the remaining amount of solid concentration left, which is given by

$$\phi_{ref} = \phi_{ref}^{init} + (v_s^{init} - v_s) \qquad (6)$$

where $v_s = C_s v_s^m$ is the volumetric fraction of solid concentration in the control volume and $v_s^{init} = C_s^{init} v_s^m$ is the initial volumetric fraction the solid (v_s^m is the molar volume). The difference between v_s and v_s^{init} address the amount of solid volumetric fraction dissolved, i.e. the amount of porosity increase in the control volume.

The updated values of ϕ_{ref} are used to compute the porosity field due to the pressure change

$$\phi = \phi_{ref}[1 - c_r(p - p_{ref})] \qquad (7)$$

where c_r is the rock compressibility, p the pressure, p_{ref} the reference pressure.

Since porosity and permeability are strongly related, the permeability field should be corrected after the dissolution of solid rock. In this study, we employ a Kozeny-Carman relationship (Kozeny, 1927; Carman, 1937):

$$\frac{K}{K^{init}} = \frac{\phi_{ref}^3 (1 - \phi_{ref}^{init})^2}{(\phi_{ref}^{init})^3 (1 - \phi_{ref})^2} \qquad (8)$$

where K and K^{init} are the current and initial permeabilities, respectively.

3. SIMULATION RESULTS

3.1. Validation against Cohen et al. (2008) Simulation Study

Here, we compare our simulation results with the simulation study performed by Cohen et al. (2008). Their study is based on a core-scale non-equilibrium model proposed in Golfier et al.(2002) . A first order, irreversible reaction in a heterogeneous reservoir for incompressible flow was modeled under isothermal conditions. A 2D carbonate block of dimensions $25 \times 40 \times 0.1$ cm is simulated with an acid injection concentration of $C_{A\beta} = 210$ kg/m^3 and stoichiometric coefficient of 1 for a first order irreversible reaction. The initial porosity of this domain is 0.36. The permeability of the model is 1 mD and a small perturbation of 5% in permeability field is introduced to mimic the micro-scale heterogeneity as shown in the Fig. 1. The fluid is injected from the left face at a constant injection rate while the pressure at the downstream boundary is kept constant. The simulation parameters are summarized in Table. 1. The variation in the type of wormhole formation with increasing velocity was obtained in Cohen's study as shown in the Fig. 2. The shape of the wormholes for a given velocity range is consistent with the experimental findings Golfier et al. (2002) and the later simulation studies Maheshwari et al. (2013). Notice that a Darcy-type model was used in Cohen et al.(2008).
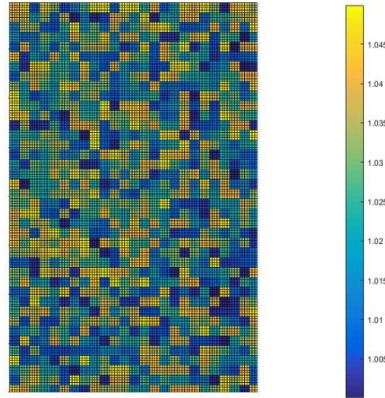

Figure 1: Fine scale heterogeneous permeability field of 1 mD + 5% with a resolution of [100x160] cells.

Parameter	Property	Value	Units
L_y	Height	0.4	m
L_x	Length	0.25	m
ϕ	Initial porosity	0.36	-
K	Permeability	1.0	mD
ΔK	Permeability perturbation	5 %	-
α	Reaction rate constant	10	$1/s$
z_{acid}^{init}	Initial acid concentration	0.001	-
z_{H2O}^{init}	Initial water concentration	0.997	-
z_{acid}^{inj}	Concentration of acid in injection	0.7500	
z_{H2O}^{inj}	Concentration of water in injection	0.2498	
p_{out}	Pressure boundary condition downstream	100	
D	Diffusivity	10^{-9}	m^2/s

Table 1: Simulation parameters.
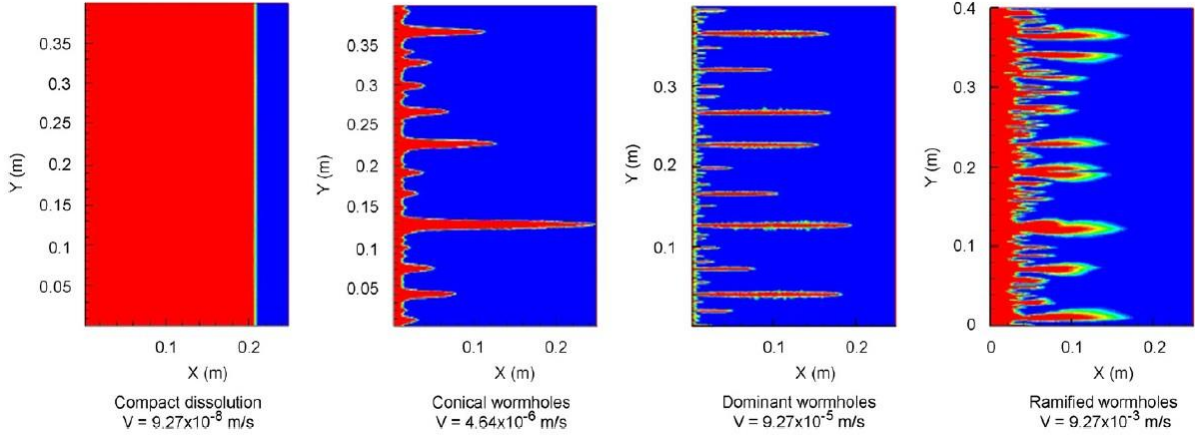
Figure 2: Cohen's simulation results. Wormhole dissolution patterns for increasing injection velocity. The red field represents region with 100% porosity. The resolution is 200×800 cells. Reprinted from Cohen et al. (2008).

With the resolution of 100×160 cells, the following results were obtained with the Darcy model after 0.7 pore volume injected (PVI), as shown in the Fig. 3. We first analyze the results in terms of the Pore Volumes for Breakthrough (PV_{BT}), which corresponds to the volume of injected acid, measured in pore volumes, which is required for wormhole at particular regime to breakthrough.

We start at low velocity regime where no wormholes observed at the front, which is the compact dissolution regime (see the first image in Fig. 3). Next, we enter the conical wormhole regime by increasing the injection velocity. In the conical regime, there is a single prominent or leading wormhole that channels most of the incoming flux. That explains much lower PV_{BT} than in the compact regime (see Fig. 4). With the increasing velocity, the wormholes start thinning due to more dominant dissolution in the tip of wormholes. This is the most effective regime for both Darcy and DBS models as can be seen in Fig. 4. On further increasing the velocity, we can observe more wormholes, carrying the influx and dissolving more rock along it. Once in the dominant regime, there are multiple wormholes without a clear leading wormhole. This slows the breakthrough as illustrated in the Fig. 4. Moving into the ramified regime, there are multiple wormholes but the wormhole tips are now smeared and the penetration into the core is much weaker and hence the PV_{BT} increases. The porosity fields corresponding to the points used in Fig. 4 are shown in Fig. 3.

$V_0 = 9.27 \cdot 10^{-8}$ m/s $\quad\quad$ $V_0 = 4.64 \cdot 10^{-6}$ m/s $\quad\quad$ $V_0 = 9.27 \cdot 10^{-5}$ m/s $\quad\quad$ $V_0 = 9.27 \cdot 10^{-3}$ m/s
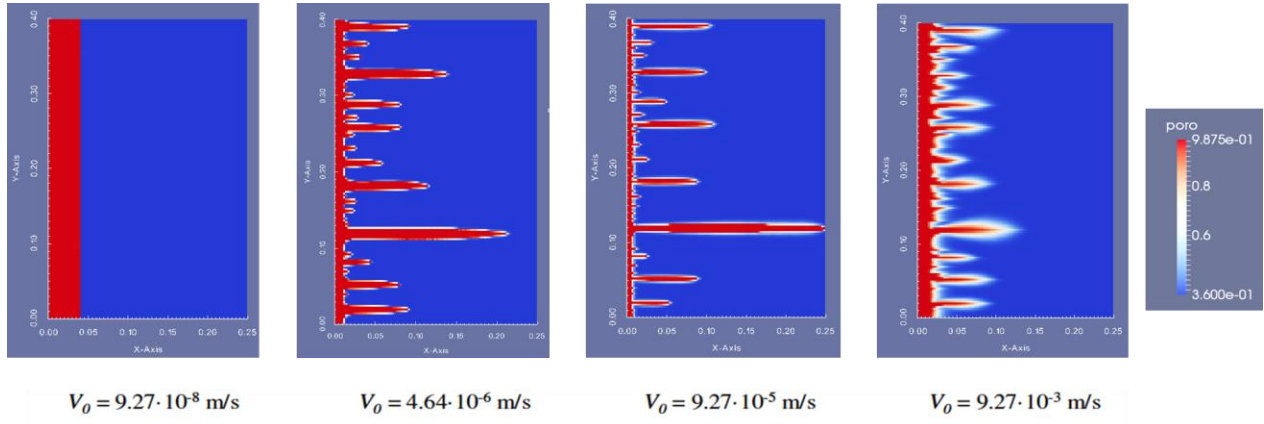
Figure 3: Darcy model simulations. Wormhole dissolution patterns for increasing injection velocity: (a) Compact Dissolution; (b) Conical Wormhole; (c) Dominant Wormhole; (d) Ramified Wormhole.
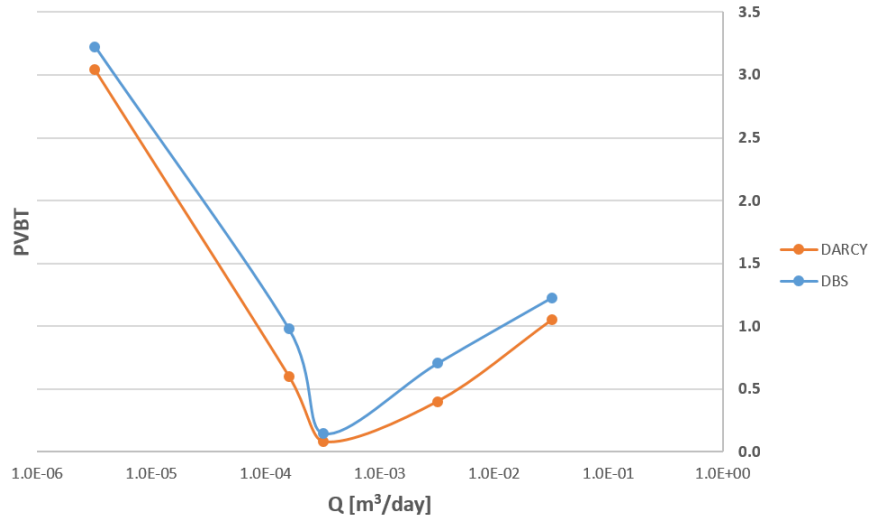

Figure 4: PV_{BT} analysis for Darcy and DBS models for the resolution of 100×160 cells.

In addition to PV_{BT} metric, we check another metric suggested by in the experimental works of McDuff et al. (2010). This metric represents the ratio of the length of the leading wormhole to the length of the average wormhole which we call γ ratio. The γ ratio has a maximum in between before the dominant regime and decreases on either side of this regime as can be seen in Fig. 5. For a low-velocity injection (compact regime) this parameter is $\gamma = 1$ as there is no wormholes. Similarly, for the high-velocity injection i.e. for ramified dissolution, there are no distinct leading wormholes and the γ ratio again close to 1 as depicted in Fig. 5. It is interesting that in this regime, the maximum is reached at the dominant regime and not corresponds to the optimal regime in terms of breakthrough (which is between the dominant and conical regimes). The average wormhole length is measured for a near breakthrough. The image analysis to obtain and count the length of wormhole was done in the public image analysis software Fiji (Schindelin et al., 2012) with simple binary operations.
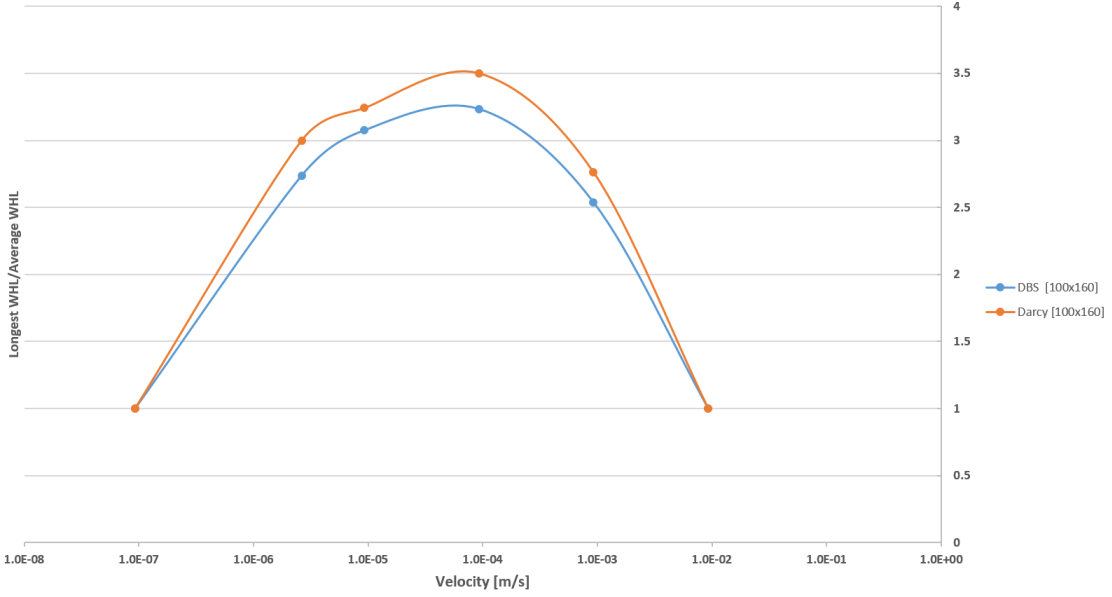
6

Figure 5: Ratio of length of the leading wormhole to the length of the average wormhole for Darcy and DBS models for the resolution of 100×160 cells.

To conclude, our simulations qualitatively reproduce the Cohen's results (Fig. 2) except for few unimportant details. While both conical and ramified regimes look quite similar, the dominant wormhole is more pronounced in Cohen's study. We can address these differences to the different solution methods and resolution. In the next section, we will perform the resolution study to address this issue.

3.2. Comparison with Darcy-Brinkman-Stokes Model

In addition, we perform a comparison between results of simulation with Darcy and DBS model. Here we employ a newly introduced implementation of a separate momentum equation in the AD-GPRS framework. In this implementation, the velocities at gridblock interfaces are used as independent variables. The details of the discretization of momentum balance equation, Eq. 4, are given in Appendix A.

The Darcy-Brinkman-Stokes model gave a result in agreement with the Darcy results as can be seen in Fig. 6. However, you can notice that the development of fingers and breakthrough moment happened much later with DBS approach than in the Darcy model as evident from the Fig. 6. The volume of the dissolved rock (red colour) in the DBS simulation after the injection of 0.7 PVI is not the same as the one in Fig. 3. We use the PV_{BT} analysis to quantify the difference. Taking a closer look at Fig. 4, which shows the differences in the PV_{BT} for Darcy and DBS models, we can establish that the Darcy model always needs fewer pore volumes for breakthrough than the DBS model. This could be understood by the fact that in the Darcy model, we ignore the dissipative viscous forces term i.e $-\mu' \Delta \vec{V}$. The DBS model takes these losses into account which plays an important role for control volumes with significantly dissolved rock. The difference in the ratio of length of the leading wormhole to the length of the average wormhole between Darcy and DBS models is shown in Fig. 5.
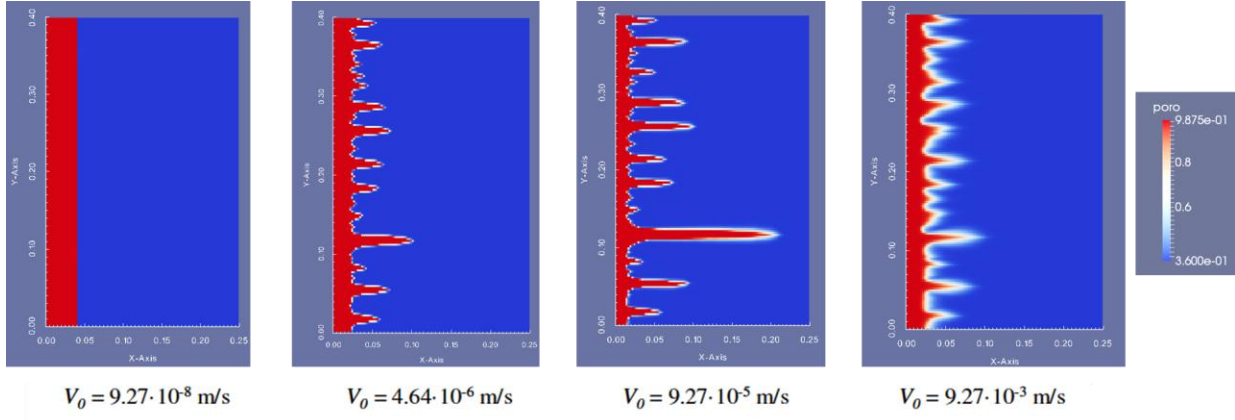
Figure 6: Darcy-Brinkman-Stokes model simulations. Wormhole dissolution patterns for increasing injection velocity: (a) Compact Dissolution; (b) Conical Wormhole; (c) Dominant Wormhole; (d) Ramified Wormhole.

3.3. Representation in Dimensionless Numbers

The considered physical phenomenon can be characterized by the two dimensionless numbers – Peclet (*Pe*) and Damkohler (*Da*) numbers. These numbers can be used to compare different wormhole models and to determine optimum operation regime in terms of these dimensionless numbers.

The Damkohler number is defined as the ratio of reaction rate to advection rate and is given by

$$Da = \frac{l\alpha}{V_o}$$

where l and V_o is the characteristic length scale and velocity, respectively. The Damkohler number gives an insight into controlling the shape of the wormhole. For instance, if the reaction rate is much larger than advection rate, the acid, flowing through the carbonate rock, dissolves it rapidly, thereby leading to a compact dissolution face (leftmost point in Fig. 7). If the reaction rate is balanced with the advection rate, an ideal operating range can be obtained i.e in the dominant wormhole regime as evident from the figure where the PV_{BT} is minimum.

In the case of optimizing the wormhole formation and growth, the following things can help us to improve the engineering of the acid job: higher permeability, sufficiently high diffusion so that the wormholes are wide enough while penetrating the rock and a higher velocity to aid it. All these three factors can be quantified as the ratio of mass transport due to convection and transport due to diffusion, which corresponds to the Peclet number given by

$$Pe = \frac{lV_o}{D}$$

In agreement with the optimization plot obtained for Damkohler number, we observe a similar shape for Peclet number. At intermediate Peclet number, the wormhole is growing fast enough and is wide enough which leads to lowest PV_{BT} as illustrated in Fig. 7.
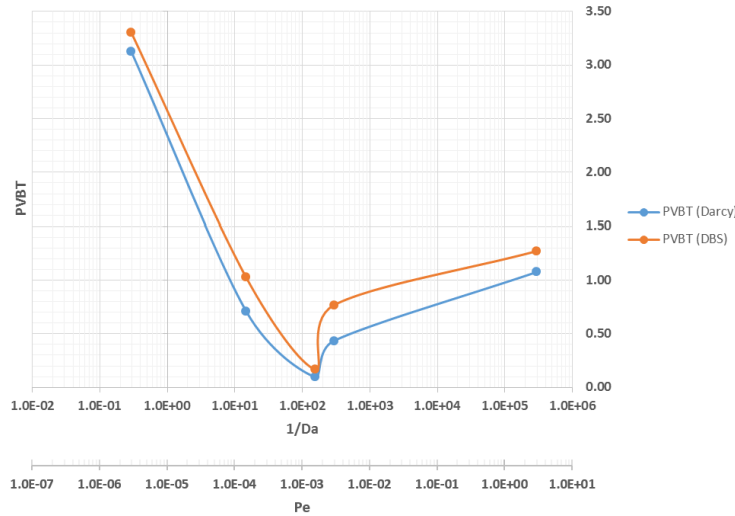
Figure 7: Analysis of PV_{BT} with changing Damkohler and Peclet number.

3.4. Numerical Convergence Study

Here we will demonstrate that our solution is numerically converged independent of the type of wormhole formation for two models for momentum equation: Darcy and Darcy-Brinkman-Stokes. We will again use PV_{BT} to better quantify the convergence of the numerical solution independent from the wormhole pattern. The impact of resolution is studied by simulating the acidization on four degrees of resolution which are subjectively classified as follows:

Very coarse	- 25×40 cells
Coarse	- 50×80 cells
Fine	- 100×160 cells
Very fine	- 200×320 cells

To reduce the influence of heterogeneity of permeability to the convergence study, the heterogeneity pattern was generated for the coarsest model and downscaled to its finer resolutions.

In Fig. 8 and Fig. 9 one can see the porosity distribution after injecting of 0.7 PVI at different resolutions for a conical wormhole regime. To quantify the differences, we repeat the PV_{BT} analysis for different flow regimes and grid resolutions (see Fig. 10). The breakthrough time is lower for a higher resolution due to the factors previously discussed. Although the finest scale used here has just 64 000 cells in comparison to 160 000 cells used by Cohen et al. (2008), you can see that this resolution is sufficient to get convergent results for this regime. As Fig.11 illustrates, the relative error with respect to the finest resolution is reduced significantly at a resolution of 100×160.
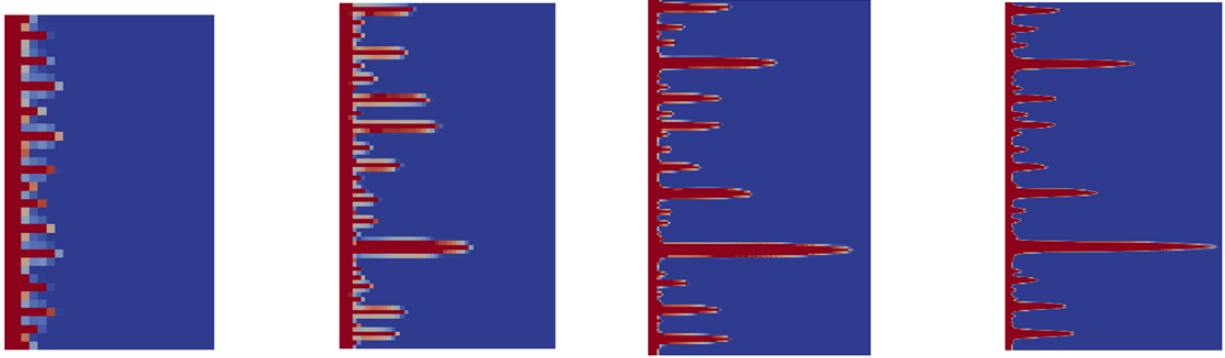
Figure 8: Darcy model – Conical wormhole ($Q = 1.6 \cdot 10^{-4}$ m^3/day) at same 0.55 PVI for (a) Very Coarse (25×40), (b) Coarse (50×80), (c) Fine (100×160), (d) Very Fine (200×320).

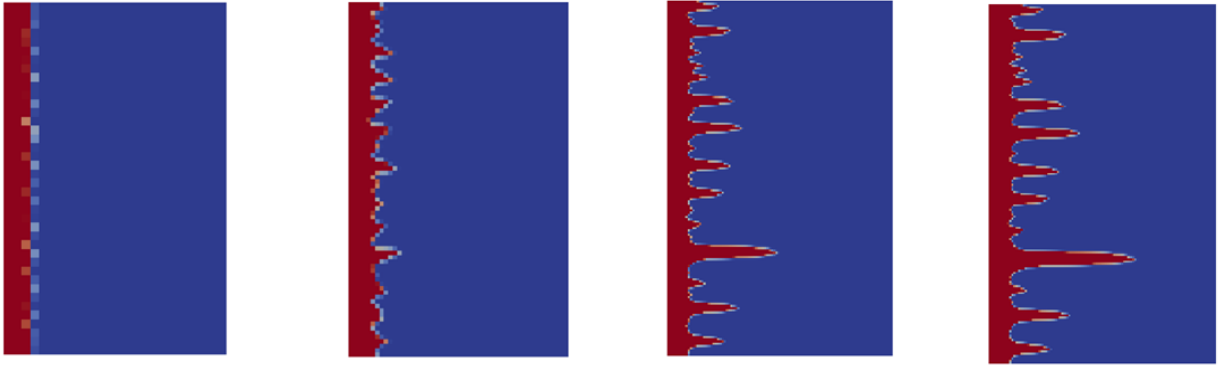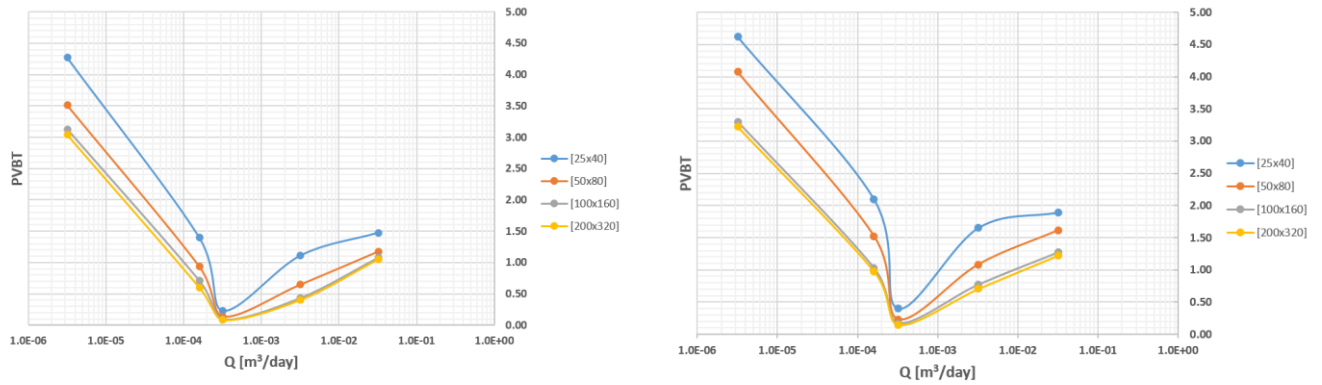**Figure 9: DBS model – Conical wormhole ($Q = 1.6 \cdot 10^{-4}$ m^3/day) at same 0.55 PVI for (a) Very Coarse (25×40), (b) Coarse (50×80), (c) Fine (100×160), (d) Very Fine (200×320).**

Figure 10: PV_{BT} analysis for different resolutions. Left: Darcy model, Right: DBS model.

Fig. 12 demonstrates the difference in previously introduced parameter γ for the mesh convergence analysis of the two models. The γ ratio plot almost overlaps for the finest resolution in our study. We can therefore conclude from Figs. 10 and 12 that the solution converges and becomes independent of the grid resolution for model with 100×160 cells and higher. This conclusion is valid for both Darcy and DBS models.
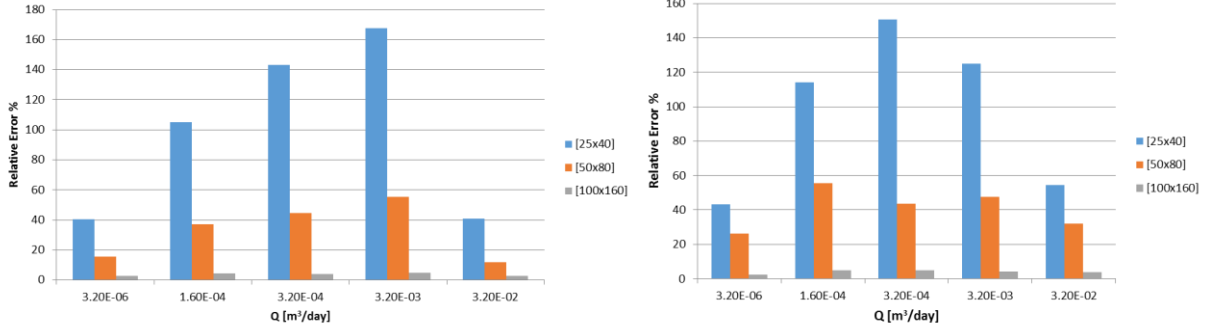
Figure 11: Relative error in PV_{BT} for Darcy model (a) and DBS model (b) with respect to the 200×320 solution.
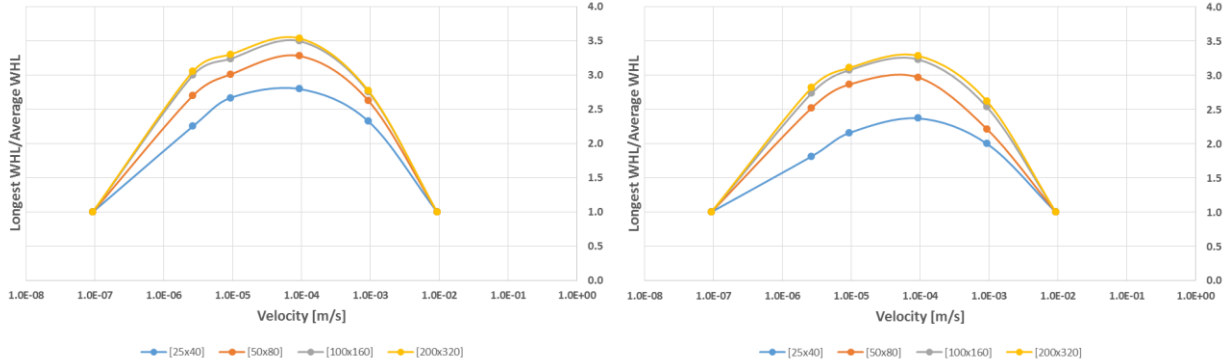

Figure 12: Ratio of length of the leading wormhole to the length of the average wormhole for (a) Darcy model (b) DBS model.

3.5. Effect of Heterogeneity

The effect of heterogeneity on the wormhole dynamics has a controversial interpretation in the published studies. In this thesis, we will try to limit the study by two factors: the growth of the most dominant wormhole with time and the number of dominant wormholes vs. the heterogeneity amplitude.

Keeping the same parameters, we increase the heterogeneity amplitude of permeability for a dominant regime. We used permeability perturbations ΔK of 5%, 10% and 20%. The porosity distributions for all three amplitudes in the case of Darcy and DBS models are shown in Fig. 13 and Fig. 14 respectively. Based on these results, there is a limited sensitivity of the wormhole distribution to the heterogeneity amplitude.
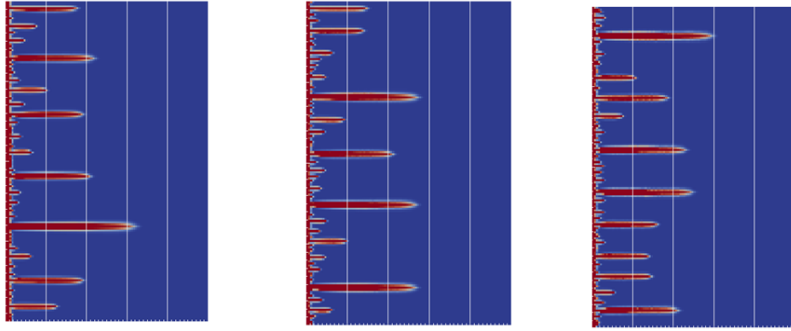
Figure 13: Porosity maps for Darcy model for permeability perturbation of 5% 10% and 20% showing several dominant wormholes.
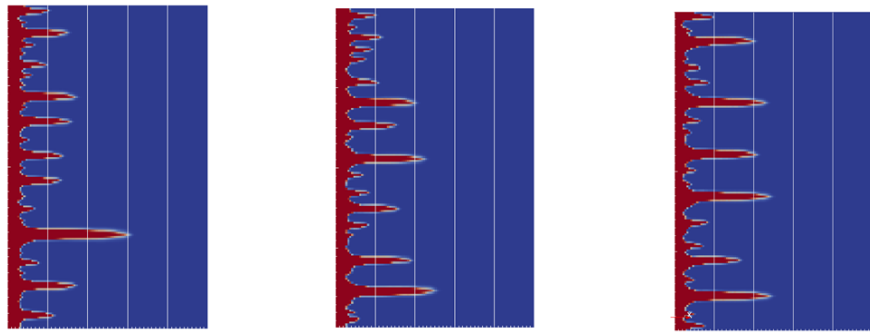

Figure 14: Porosity maps for DBS model for permeability perturbation of 5% 10% and 20%.

However, this conclusion is changing if we look into the sensitivity of dominant wormhole length as function of time. From Fig. 15 it is clear that for $\Delta K = 20\%$ the length of the leading wormhole lags behind for cases with lower amplitude. This behavior can be understood by taking a closer look the porosity maps in Fig. 15. As the heterogeneity amplitude increases, the number of wormholes increases which leads to less competition between the wormholes. As a result, the breakthrough time is changing proportional to the heterogeneity amplitude.
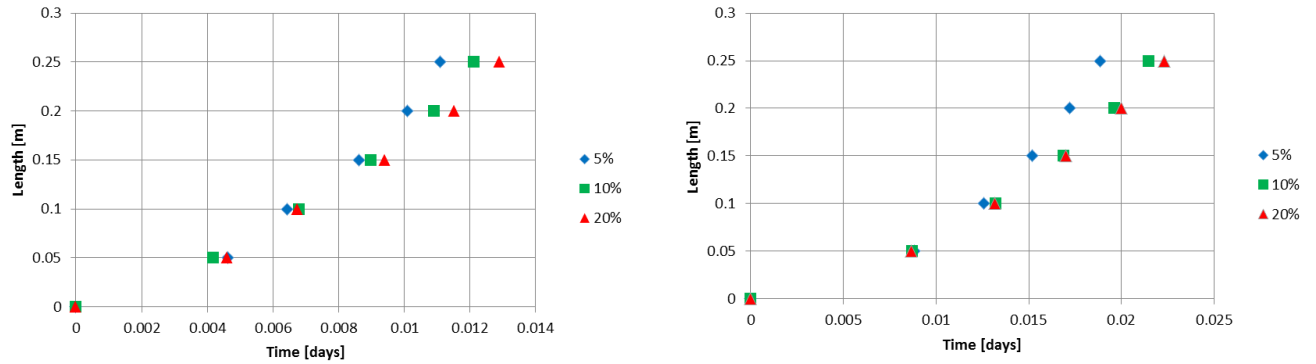

Figure 15: Wormholing dynamics for Darcy (left) and DBS (right) models for permeability perturbation of 5%, 10% and 20%.

4. CONCLUSION

In this research, the problem of acidization was studied using two different modeling approaches implemented in AD-GPRS framework. The first is the conventional Darcy modeling using the volume based averaging of Darcy's law. The second modeling approach involved a single domain micro-continuum approach i.e. the hybrid modeling with the Darcy-Brinkman-Stokes (DBS) approach. These models were validated using the published results. Distinct differences were observed in terms of the wormhole shapes between Darcy and DBS models. In terms of Pore Volume for Breakthrough (PV_{BT}), the Darcy model gave consistently lower PV_{BT} than the DBS model. Physically, it can be attributed to the discounting of dissipative viscous forces in the Darcy model.

A further analysis on the resolution indicates a dependency of numerical results. A mesh convergence analysis confirmed the minimum grid resolution as 100×160 cells to capture the phenomenon accurately. Translation of the results into dimensionless numbers gave us an optimal regime in terms of Damkohler and Peclet numbers, though there is a debate on the definitions of optimal conditions and several researchers deviated from these conventional dimensionless numbers to formulate other variables and report the best operating conditions. Finally, another factor affecting the wormhole propagation was found to be the amplitude of the rock heterogeneity. A larger perturbation influenced the number of wormholes formed and thereby affecting the breakthrough time.

5. ACKNOWLEDGMENTS

APPENDIX

A. Discretization of Momentum Equation

Here we briefly describe how we discretize the momentum balance, Eq. 4, see, e.g. (Olshanskii et al., 2013; Perot, 2000; Perot and Nallapati, 2003) for details. For simplicity of the description we assume scalar absolute permeability and constant viscosity.

We start from introducing the velocity unknowns: $q_f = \mathbf{V}\mathbf{n}_f A_f$ which are phase fluxes through cell faces. Here n_f is the face normal and A_f is the face surface.

For single-phase Darcy's law we usually have the following projection on the face (TPFA scheme):

$$q_f = -\frac{1}{\mu}(K\nabla p)_f \mathbf{n}_f A_f = -\frac{1}{\mu}T_f(\Delta p)_f \tag{9}$$

where $T_f = A_f K_f$ is the transmissibility $(K_f = 2/(d_1/K_1 + d_2/K_2))$, $(\Delta p)_f = p_1 - p_2$ is the pressure difference.

Full projection of Eq. 4 has the form

$$-\frac{1}{\mu}T_f(\Delta p)_f + \frac{1}{\phi_f}(K\Delta \mathbf{V})_f \mathbf{n}_f A_f - q_f = 0 \tag{10}$$

where $\phi_f = \frac{(\phi_1 + \phi_2)}{2}$ is the porosity on the face. In Eq. 10, the main issue is to approximate the Brinkman term, which is done with the following algorithm:

    1.   Cell-centered velocity can be reconstructed from q_f as following

$$\mathbf{V}_c = \frac{1}{v_\Omega} \sum_{f \in \partial\Omega} q_f (\mathbf{x}_f - \mathbf{x}_c) \tag{11}$$

where v_Ω is the cell volume, $\mathbf{x}_c$ is the position of the cell center, $\mathbf{x}_f$ are the positions of centers of the cell faces.

2. Compute the velocity Laplacian in the cell center using the two-point approximation

$$(\Delta\mathbf{V})_c = \nabla.(\nabla v) = \frac{1}{v_\Omega} \sum_{f \in \partial\Omega} (\nabla v)_f \mathbf{n}_f A_f = \frac{1}{v_\Omega} \sum_{f \in \partial\Omega} T_f^v (\Delta v_c)_f \tag{12}$$

where $(\Delta\mathbf{V}_c)_f = \mathbf{V}_{cf} - \mathbf{V}_c$ and $T_f^v = A_f / (d_1 + d_2)$

3. Finally project the $(\Delta\mathbf{V})_c$ to the face

$$(K\Delta\mathbf{V})_f \mathbf{n}_f A_f = (\Delta\mathbf{V})_f \mathbf{n}_f A_f K_f = \left[(\Delta\mathbf{V})_{c,1} (\mathbf{x}_f - \mathbf{x}_1) - (\Delta\mathbf{V})_{c,2} (\mathbf{x}_f - \mathbf{x}_2) \right] T_f \tag{13}$$

If no-slip boundary condition, $\mathbf{V}|_\Gamma = \mathbf{0}$ is required, it simply should be accounted in the Laplacian computation (Eq. 12), and for $f \in \Gamma$ we have

$$T_f^v (\Delta\mathbf{V}_c)_f = -T_f^v \mathbf{V}_c \tag{14}$$

where

$$T_f^v = \frac{A_f}{d} \tag{15}$$

d is the distance to the face from the cell center.

REFERENCES

AD-GPRS. Automatic Differentiation General Purpose Research Simulator (AD-GPRS), (2017). https://supri-b.stanford.edu/research-areas/ad-gprs.

L.A. Barrios, J.E. Quijano, R.E. Romero, H. Mayorga, M. Castro, and J. Caldera. Enhanced permeability by chemical stimulation at the Berlin geothermal field, el salvador. In *Transactions - Geothermal Resources Council*, pages 73–78, (2002).

P Bousquet-Melou, B Goyeau, Michel Quintard, F Fichot, and D Gobin. Average momentum equation for interdendritic flow in a solidifying columnar mushy zone. *International journal of heat and mass transfer*, **45(17)**: 3651–3665, (2002).

HC Brinkman. A calculation of the viscous force exerted by a flowing fluid on a dense swarm of particles. *Applied Scientific Research*, **1(1)**:27–34, (1949).

Philip Crosbie Carman. Fluid flow through granular beds. *Transactions-Institution of Chemical Engineeres*, **15**:150–166, (1937).

Charles Edouard Cohen, Didier Ding, Michel Quintard, and Brigitte Bazin. From pore scale to wellbore scale: Impact of geometry on wormhole growth in carbonate acidization. *Chemical Engineering Science*, **63(12)**: 3088–3099, (2008).

Curtis Crowe and Ron Thomas. Trends in matrix acidizing. *Oilfield Review series, Schlumberger*, **10**, (1992).

Henry Darcy. Les fontaines publique de la ville de dijon. *Dalmont, Paris*, 647, (1856).

Robert C Earlougher Jr. Advances in well test analysis, henry l. *Doherty series, Monograph*, **5**, (1977).

Yaqing Fan, Louis Durlofsky, Hamdi A Tchelepi, et al. Numerical simulation of the in-situ upgrading of oil shale. *SPE Journal*, **15(02)**:368–381, (2010).

Yaqing Fan, Louis J Durlofsky, and Hamdi A Tchelepi. A fully-coupled flow-reactive-transport formulation based on element conservation, with application to co 2 storage simulations. *Advances in Water Resources*, **42**: 47–61, (2012).

Sara F Farshidi, Yaqing Fan, Louis J Durlofsky, Hamdi A Tchelepi, et al. Chemical reaction modeling in a compositional reservoir-simulation framework. In *SPE Reservoir Simulation Symposium*. Society of Petroleum Engineers, (2013).

Sara Forough Farshidi. *Compositional Reservoir Simulation-based Reactive-transport Formulations, with Application to CO_2 Storage in Sandstone and Ultramafic Formations*. PhD thesis, Stanford University, (2016).

F Golfier, C ZArcone, B Bazin, R Lenormand, D Lasseux, and M Quintard. On the ability of a darcy-scale model to capture wormhole formation during the dissolution of a porous medium. *Journal of fluid Mechanics*, **457**:213–254, (2002).

B Goyeau, D Lhuillier, D Gobin, and MG Velarde. Momentum transport at a fluid–porous interface. *International Journal of Heat and Mass Transfer*, **46(21)**:4071–4081, (2003).

CT Hsu and P Cheng. Thermal dispersion in a porous medium. *International Journal of Heat and Mass Transfer*, **33(8)**:1587–1597, (1990).

J.G. Jaimes-Maldonado and R. Snchez-Velasco. Acid stimulation of production wells in las tres vrgenes geothermal field, bcs, mxico. In *Transactions - Geothermal Resources Council*, volume **27**, pages 699–705, (2003).

Leonard Kalfayan. *Production enhancement with acid stimulation*. Pennwell Books, (2008).

Josef Kozeny. Uber kapillare leitung der wasser in boden. *Royal Academy of Science, Vienna, Proc. Class I*, **136:**271–306, (1927).

P Maheshwari, RR Ratnakar, N Kalia, and V Balakotaiah. 3-d simulation and analysis of reactive dissolution and wormhole formation in carbonate rocks. *Chemical Engineering Science*, **90:**258–274, (2013).

Darren McDuff, Chris E Shuchart, Shalawn Jackson, Dieter Postl, James Seay Brown, et al. Understanding wormholes in carbonates: Unprecedented experimental scale and 3-d visualization. In *SPE Annual Technical Conference and Exhibition*. Society of Petroleum Engineers, (2010).

Donald A Nield and Adrian Bejan. *Convection in porous media*, Volume **3**. Springer, (2006).

J Alberto Ochoa-Tapia and Stephen Whitaker. Heat transfer at the boundary between a porous medium and a homogeneous fluid: the one-equation model. *Journal of Porous Media*, **1(1)**, (1998).

Maxim A Olshanskii, Kirill M Terekhov, and Yuri V Vassilevski. An octree-based solver for the incompressible navier–stokes equations with enhanced stability and low dissipation. *Computers & Fluids*, **84:**231–246, (2013).

Blair Perot. Conservation properties of unstructured staggered mesh schemes. *Journal of Computational Physics*, **159(1):**58–89, (2000).

Blair Perot and Ramesh Nallapati. A moving unstructured staggered mesh method for the simulation of incompressible free-surface flows. *Journal of Computational Physics*, **184(1):**192–214, (2003).

Sandrine Portier, François-David Vuataz, Patrick Nami, Bernard Sanjuan, and André Gérard. Chemical stimulation techniques for geothermal wells: experiments on the three-well egs system at soultz-sous-forêts, france. *Geothermics*, **38(4):**349–359, (2009).

Ruslan Rin. *Implicit Coupling Framework for Multi-Physics Reservoir Simulation*. PhD thesis, Stanford University, (2017).

Ruslan Rin, Pavel Tomin, Timur Garipov, Denis Voskov, Hamdi Tchelepi, et al. General implicit coupling framework for multi-physics problems. In *SPE Reservoir Simulation Conference*. Society of Petroleum Engineers, (2017).

Olaf Schenk and Klaus Gärtner. Solving unsymmetric sparse systems of linear equations with pardiso. *Future Generation Computer Systems*, **20(3):**475–487, (2004).

Johannes Schindelin, Ignacio Arganda-Carreras, Erwin Frise, Verena Kaynig, Mark Longair, Tobias Pietzsch, Stephan Preibisch, Curtis Rueden, Stephan Saalfeld, Benjamin Schmid, et al. Fiji: an open-source platform for biological-image analysis. *Nature methods*, **9(7):**676–682, (2012).

Cyprien Soulaine and Hamdi A Tchelepi. Micro-continuum approach for pore-scale simulation of subsurface processes. *Transport in Porous Media*, **113(3)**:431–456, (2016).

Cyprien Soulaine, Filip Gjetvaj, Charlotte Garing, Sophie Roman, Anna Russian, Philippe Gouze, and Hamdi A Tchelepi. The impact of sub-resolution porosity of x-ray microtomography images on the permeability. *Transport in Porous Media*, **113(1):**227–243, (2016).

Cyprien Soulaine, Sophie Roman, Anthony Kovscek, and Hamdi A Tchelepi. Mineral dissolution and wormholing from a pore-scale perspective. *Journal of Fluid Mechanics*, **827:**457–483,(2017).

K Vafai and CL Tien. Boundary and inertia effects on flow and heat transfer in porous media. *International Journal of Heat and Mass Transfer*, **24(2)**:195–203, (1981).

Kambiz Vafai. *Handbook of porous media*. CRC Press, (2015).

Denis V. Voskov and Hamdi A. Tchelepi. Comparison of nonlinear formulations for two-phase multi-component EoS based simulation. *Journal of Petroleum Science and Engineering*, **8283**:101 – 111,(2012). ISSN 0920-4105. doi: http://dx.doi.org/10.1016/j.petrol.2011.10.012.

George A Xydis, Evanthia A Nanaki, and Christopher J Koroneos. Low-enthalpy geothermal resources for electricity production: A demand-side management study for intelligent communities. *Energy policy*, **62:**118–123, (2013).